

Role of on-site Coulomb energy and negative-charge transfer in a Dirac semi-metal NiTe₂

A. R. Shelke,¹ C. -W. Chuang,² S. Hamamoto,³ M. Oura,³ M. Yoshimura,¹ N. Hiraoka,¹ C.-N. Kuo,^{4,5,6} C.-S. Lue,^{4,5,6} A. Fujimori,^{1,7,8} and A. Chainani¹

¹National Synchrotron Radiation Research Center, Hsinchu 300092, Taiwan

²Experimentelle Physik VII, Universität Würzburg, Am Hubland, D-97074 Würzburg, Germany

³RIKEN SPring-8 Center, Hyogo 679-5148, Japan

⁴Program on Key Materials, Academy of Innovative Semiconductor and Sustainable Manufacturing (AISSM),

National Cheng Kung University, Tainan 70101, Taiwan

⁵Department of Physics, National Cheng Kung University, Tainan 70101, Taiwan

⁶Taiwan Consortium of Emergent Crystalline Materials,

National Science and Technology Council, Taipei, Taiwan

⁷Department of Physics, The University of Tokyo, 7-3-1 Hongo, Bunkyo-ku, Tokyo 113-0033, Japan

⁸Center for Quantum Technology, and Department of Physics,

National Tsing Hua University, Hsinchu 300044, Taiwan

(Dated: February 24, 2026)

Angle-resolved photoemission spectroscopy (ARPES) combined with band structure calculations have shown that the layered transition metal dichalcogenide(TMD) NiTe₂ is a type-II Dirac semimetal. However, conflicting conclusions were reported regarding the role of electron correlations in NiTe₂. We study core-levels and valence band electronic structure of single crystal NiTe₂ using soft and hard x-ray photoemission spectroscopy(SXPES, HAXPES), X-ray absorption spectroscopy(XAS) and Ni 2*p*–3*d* Resonant-PES to quantify electronic parameters in NiTe₂. The Ni 3*d* on-site Coulomb energy (U_{dd}) is quantified from measurements of the Ni 3*d* single particle density of states(DOS) and the two-hole correlation satellite. The Ni 2*p* core level and *L*-edge XAS spectra are analyzed by charge-transfer (CT) cluster model calculations using the experimental U_{dd} , and it shows that NiTe₂ exhibits a negative CT energy Δ . A comparative analysis of NiO *L*-edge XAS confirms its well-known strongly correlated CT insulator character, with a larger U_{dd} and positive Δ . The *d*-*p* hybridization strength T_{eg} for NiTe₂<NiO, and shows that T_{eg} is not responsible for reducing U_{dd} in NiTe₂ compared to NiO. The negative- Δ and a reduced U_{dd} leads to the increase in d^n count on the Ni site in NiTe₂ by nearly one electron. However, importantly, since $U_{dd}>|\Delta|$, a finite repulsive U_{dd} results in pushing *d*-states away from Fermi level and this is required to make NiTe₂ a moderately correlated Dirac semi-metal with band inversion in the *p*-*p* type lowest energy excitations.

I. INTRODUCTION

The fascinating transport properties and electronic structure of topological insulators (TIs) predicted by theory^{1–7} and their experimental validation^{8,9} established the field of TIs in condensed matter. In particular, (i) transport measurements of a Quantum Spin Hall insulator proved existence of a pair of gapless helical edge-states in HgTe/(Hg,Cd)Te quantum wells⁸, and (ii) ARPES showed Dirac-type metallic surface state bands inside a bulk charge gap induced by spin-orbit coupling (SOC) with band inversion in Bi_{1–*x*}Sb_{*x*}⁹. While inverted band gaps in substituted semiconductors leading to Dirac/Weyl type bands in the gap was recognized earlier^{10,11}, Dirac cones and band inversions were soon reported in several materials like Bi₂Se₃, Sb₂Te₃, etc.^{12–14} confirming their TI character.

Similarly, the 3-dimensional (3D) Weyl semimetal (WSM) was predicted to show a band structure with a pair of Dirac/Weyl nodes of opposite chirality, separated in momentum(*k*)-space¹⁵. WSMs were also predicted to show a Drude weight vanishing as T^2 and it was confirmed by experiments¹⁶. ARPES studies showed characteristic Fermi arcs connecting the Dirac/Weyl nodes in TaAs^{17,18} and NbP¹⁹. The WSMs require broken time-reversal symmetry and/or broken inversion symmetry²⁰. In contrast, the Dirac semimetals(DSMs) form in the presence of time-reversal and inversion symmetries^{21,22}. They are of 2 types: Type I DSMs obey

Lorentz symmetry and show regular Dirac-type linear dispersions along all 3 directions in *k*-space as seen in Na₃Bi^{29,30} and Cd₃As₂^{31,32}; Type II DSMs violate Lorentz symmetry and show tilted Dirac cones with a Dirac point at which an electron and a hole pocket touch each other^{21,22}.

Many layered TMDs have shown Type II DSM behavior^{22,33–44} and in this work, we focus on the electronic structure of NiTe₂. ARPES studies showed a bulk Type-II Dirac point in NiTe₂ lying \sim 20-68 meV above E_F by three groups^{39–41}, while another group reported it to lie 150 meV below E_F ⁴². NiTe₂ also shows surface states at E_F , and another Dirac-like crossing lies far (\sim 1.5 eV) below E_F ^{39–42,44}. However, while three studies on NiTe₂ using ARPES and band structure calculations had ruled out correlation effects in NiTe₂^{39–41}, two very recent studies have concluded the importance of correlations for the Te 5*p* derived bands in NiTe₂^{43,44}. Fischer et al.⁴³ carried out DFT calculations and calculated many-body effects within the GW approximation. They found improvement in the Te 5*p* bands with an increase in Dirac carrier velocity exceeding 100% and emphasized the subtle influence of electronic interactions on band structure. Bhatt et al.⁴⁴ used LDA+U (with $U = 5$ eV) and concluded that the topological Te 5*p* surface states lying \sim 1.5 eV below E_F can be described only by including U . Surprisingly, there is no discussion of the role of correlation effects in Ni 3*d* states of NiTe₂ to date.

Since Ni is divalent in NiTe₂ as the Te atoms are dimerized

(Te_2^-)^{45,46}, it is important to consider the example of divalent NiO which is known to be a strongly correlated CT insulator. Thus, Ni^{2+} states in NiTe_2 may also be correlated, and we use the case of NiO as a benchmark to compare it with correlation effects in NiTe_2 . However, it is known that NiTe_2 is a Pauli paramagnetic metal⁴⁷ and may as well be less correlated than NiO. On the other hand, bulk sensitive dHvA experiments showed that individual bands had to be shifted in a somewhat ad-hoc manner (one with an energy shift of -60 meV, and another with a shift of +100 meV) to match with measured dispersions. Also, calculated and measured values of light and nearly isotropic effective masses showed discrepancies. It was concluded that DFT calculations failed to capture the finer details of the band structure of NiTe_2 ⁴⁷.

While materials like NiTe_2 are called semimetals because they show small electron- and hole-pockets, their actual conductivities are quite high due to high carrier mobilities. For example, NiTe_2 exhibits a very high conductivity of $\sigma(T = 2 \text{ K}) \sim 1.0 \times 10^6 \text{ S/m}$ ²³. Magnetic susceptibility of NiTe_2 does not show evidence for magnetic ordering down to $T = 2 \text{ K}$, but is Pauli paramagnetic as mentioned above^{24,47}. It is also known that the NiTe_{2-x} series exhibits pressure-induced superconductivity²⁵. A giant Josephson diode effect in Josephson junctions formed using NiTe_2 was also reported recently²⁶. NiTe_{2-x} nanomaterials also work as electrocatalysts for hydrogen evolution reaction^{23,27}. In a very recent study, it was shown that NiTe_2 is a topological superconductor with a very low $T_C = 261 \text{ mK}$ ²⁸. Thus, NiTe_2 is important in terms of fundamental and applied properties.

In this work, we carry out SXPES, HAXPES, XAS and Ni $2p - 3d$ resonant PES to determine electronic parameters in NiTe_2 . We quantify U_{dd} in the Ni $3d$ states using experimental Ni $3d$ single particle DOS and the two-hole correlation satellite. A comparative analysis using CT cluster model calculations for L -edge XAS shows that $U_{dd} = 3.7 \text{ eV}$ and $\Delta = -2.8 \text{ eV}$ for NiTe_2 , while $U_{dd} = 7.0 \text{ eV}$ and $\Delta = 6.0 \text{ eV}$ for NiO. The obtained values of d - p hybridization strength T_{eg} indicate it is smaller for NiTe_2 compared to NiO. Since $U_{dd} > |\Delta|$, it indicates the important role of a moderate repulsive U_{dd} in making NiTe_2 a topological metal with $p \rightarrow p$ type lowest energy excitations in the Zaanen-Sawatzky-Allen (ZSA) scheme⁴⁸.

II. METHODS

Synthesis and structure characterization: Single crystals of NiTe_2 were prepared by the chemical vapor transport method, using iodine as the transport agent⁴⁹. High-purity Ni (99.95%) and Te (99.999%) powders were mixed with iodine, sealed in an evacuated quartz tube, and heated for 10 days in a two-zone furnace. Finally, the quartz tube was quenched into an ice-water bath from the growth temperature of 800°C. The obtained single crystals are hexagonal in shape with typical dimensions of 4 mm×4 mm×0.5 mm. The crystal structure was characterized using powder X-ray diffraction (XRD) (Bruker D2 phaser diffractometer) with Cu-K α radiation. The single crystal quality was confirmed and crystallization directions were identified by the Laue diffraction method (Photonic

Science). The XRD results confirmed the 1T-CdI₂-type trigonal structure (space group of P3m1 (No. 164)) with the flat-surfaces corresponding to the (001) plane. The obtained lattice parameters of NiTe_2 are $a = b = 3.853 \text{ \AA}$ and $c = 5.260 \text{ \AA}$. These values are very close to reported values of $a = b = 3.843 \text{ \AA}$ and $c = 5.266 \text{ \AA}$ ⁵⁰.

Electron spectroscopy: HAXPES core levels and valence band measurements were carried out at BL-12XU, Taiwan Beamline in SPring-8, Japan, using linearly polarized x-ray beam with incident photon energy $h\nu = 6.5 \text{ keV}$. Liquid He closed cycle cryostat was used to cool down the sample to $T = 25 \text{ K}$. The E_F of Au thin film was measured at 25 K to calibrate the binding energy (BE) scale and determine the total energy resolution ($\Delta E = 270 \text{ meV}$) from a fit to the Au film Fermi edge. NiTe_2 single crystal was cleaved using a top-post in ultra-high vacuum (UHV) at $5.5 \times 10^{-9} \text{ mbar}$ in the preparation chamber and then quickly transferred to the main chamber at $7.0 \times 10^{-10} \text{ mbar}$ for the measurements. Soft X-ray PES (SXPES) core level and valence band, XAS and $2p - 3d$ resonance PES measurements were carried out at BL-17SU, RIKEN beamline in SPring-8, Japan, using a circularly polarized X-ray beam. The Ni $L_{3,2}$ -edge and Te $M_{5,4}$ -edge XAS measurements were carried out in total electron yield mode. SXPES core levels and valence band measurements were carried out with incident photon energy $h\nu = 1.5 \text{ keV}$. A Liquid N₂ flow-type cryostat was used to cool the sample down to 80 K. The total energy resolution for SXPES was set to $\Delta E = 220\text{-}400 \text{ meV}$ for $h\nu = 700 \text{ eV} - 1.5 \text{ keV}$, as obtained from fits to the Au Fermi edge (E_F) measured with $h\nu = 700 \text{ eV}$ and 1.5 keV at $T = 80 \text{ K}$. Sample was cleaved in the main chamber at a UHV better than $1.0 \times 10^{-10} \text{ mbar}$. The resonant PES spectra were normalized at the Te $4d_{5/2,3/2}$ core level peaks.

Cluster-model calculations: The Ni $L_{3,2}$ -edge XAS and Ni $2p$ PES core level spectra were calculated using a charge transfer multiplet cluster model with the QUANTY code⁵¹⁻⁵³. A NiL₆ cluster with divalent Ni^{2+} ion ($3d^8$) and 6 ligand(L) atoms of Te in octahedral symmetry (O_h) was used to calculate the spectra. The initial state consists of a linear combination of $|3d^8\rangle$, $|3d^9 \underline{L}^1\rangle$ and $|3d^{10} \underline{L}^2\rangle$ states, where \underline{L} corresponds to hole in ligand states. The ground-state is obtained by diagonalizing the Hamiltonian matrix in terms of the basis states $|3d^8\rangle$, $|3d^9 \underline{L}^1\rangle$ and $|3d^{10} \underline{L}^2\rangle$ states. The results also provide the coefficients of the basis states in the ground state. The contributions of each basis state in the ground state is then obtained as the square of its coefficient. A check on the validity of the calculations is confirmed by the sum of the percentages which add up to 100%. The value of U_{dd} was fixed to 3.7 eV as obtained from the Cini-Sawatzky analysis, while Δ , the hybridization strength (T_{eg} and $T_{2g} = T_{eg}/2$) and the crystal field splitting $10Dq$ were varied to obtain calculated spectra close to experimental spectra. The calculated spectra were obtained by convoluting the discrete final states by broadening it with a Lorentzian function for lifetimes and a Gaussian function for the experimental spectral width.

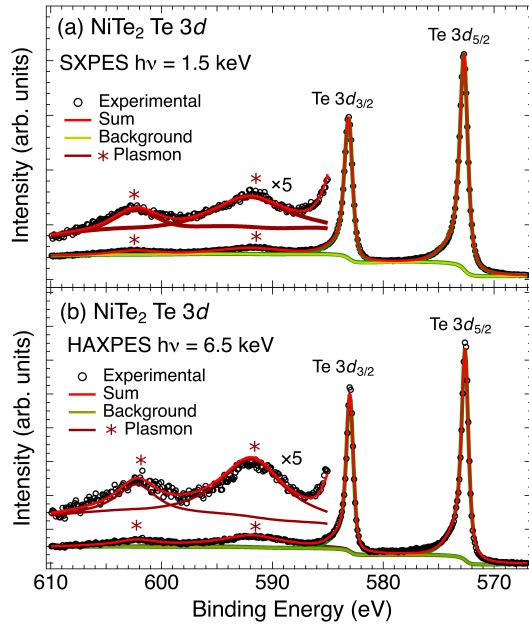


FIG. 1. Least-squares fitting of Te 3d core levels of NiTe₂ single-crystal measured at $T = 80$ K with $h\nu = 1.5$ keV (SXPES) and at $T = 20$ K with $h\nu = 6.5$ keV (HAXPES)

TABLE I. Fitting parameters of Te 3d core levels of NiTe₂ single-crystal measured using SXPES and HAXPES techniques

Fit component	Binding Energy (eV)	FWHM (eV)
SXPES		
Te 3d _{5/2}	572.72	0.82
Te 3d _{3/2}	583.13	0.88
Te 3d _{5/2} Plasmon	591.90	7.5
Te 3d _{3/2} Plasmon	602.32	4.5
HAXPES		
Te 3d _{5/2}	572.62	0.72
Te 3d _{3/2}	583.01	0.74
Te 3d _{5/2} Plasmon	591.82	7.0
Te 3d _{3/2} Plasmon	602.21	4.5

III. RESULTS AND DISCUSSION

Figures 1(a) and (b) show the Te 3d core levels of NiTe₂ measured using SXPES and HAXPES, respectively. The spectra show two sharp single peaks for Te 3d_{5/2} and Te 3d_{3/2} main peaks and weak satellite features at higher BEs. A least-squares fitting to the Te 3d_{5/2} and Te 3d_{3/2} main peaks and weak features is superimposed as full lines on the experimental spectra (empty circles). The main peaks were fitted with single asymmetric Voigt functions, and the weak features could be fitted with symmetric Gaussian functions. The peak BEs and FWHMs are listed in Table I. The Te 3d_{5/2} and Te 3d_{3/2} main peaks are at 572.72 eV ± 0.1 eV and at 583.13 eV ± 0.1 eV in SXPES and HAXPES spectra. The observed BE values are very consistent with reported values of Te 3d core levels of NiTe₂^{46,56}. The sharp single main peaks of Te

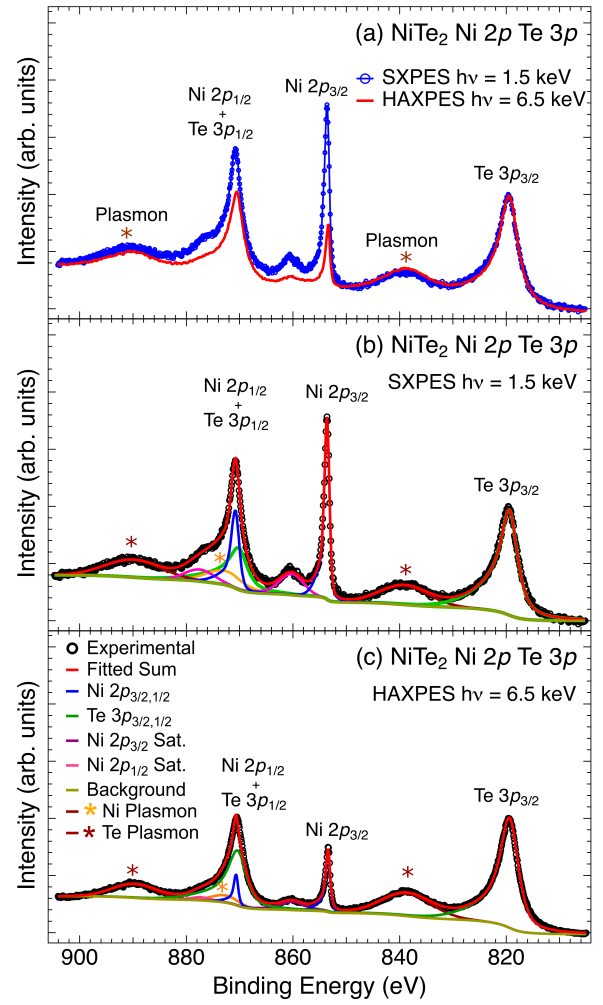


FIG. 2. (a) Ni 2p and Te 3p core level spectra of NiTe₂ single-crystal measured at $T = 80$ K with $h\nu = 1.5$ keV (SXPES) and at $T = 20$ K with $h\nu = 6.5$ keV (HAXPES). The spectra are normalized at the Te 3p_{3/2} main peak. (b) Least squares fitting of Ni 2p and Te 3p core levels of NiTe₂ measured with $h\nu = 1.5$ keV (SXPES) and (c) Least squares fitting of Ni 2p and Te 3p core levels of NiTe₂ measured with $h\nu = 6.5$ keV (HAXPES).

3d_{5/2} and Te 3d_{3/2} and absence of any feature ≈ 3.0 eV above the main peaks indicates absence of oxidation in SXPES and HAXPES spectra⁵⁶. Further, the broad low intensity features are both positioned at ~ 19.7 eV ± 0.1 eV higher BEs than the main peaks and suggests they originate from plasmon excitations. We confirm their plasmonic origin by measuring Te 3p SXPES and HAXPES core levels which also show weak satellite features at ~ 19.7 eV ± 0.1 eV higher BEs from the main peaks in Fig. 2, as discussed in the following.

Figure 2(a) shows the Ni 2p and Te 3p core level range from 812 - 900 eV BE measured with HAXPES ($h\nu = 6.5$ keV) and SXPES ($h\nu = 1.5$ keV). The spectra show three high intensity peaks instead of the expected four peaks: Ni 2p_{3/2}, Ni 2p_{1/2}, Te 3p_{3/2} and Te 3p_{1/2}, together with weak features. The spectra are normalized at the lowest BE peak at 819.4 eV BE which corresponds to the Te 3p_{3/2} main peak. The

TABLE II. Fitting parameters of Ni $2p$ and Te $3p$ core levels of NiTe₂ single-crystal measured using SXPES and HAXPES techniques

Fit component	Binding Energy (eV)	FWHM (eV)
SXPES		
Ni $2p_{3/2}$	853.62	1.10
Ni $2p_{1/2}$	870.86	1.70
Te $3p_{3/2}$	819.44	3.5
Te $3p_{1/2}$	870.24	3.5
Ni $2p_{3/2}$ Satellite	860.30	5.18
Ni $2p_{1/2}$ Satellite	877.51	6.5
Ni $2p_{3/2}$ Plasmon	872.80	8.1
Te $3p_{3/2}$ Plasmon	838.66	10.82
Te $3p_{1/2}$ +Ni $2p_{1/2}$ Plasmon	889.78	12.39
HAXPES		
Ni $2p_{3/2}$	853.43	0.97
Ni $2p_{1/2}$	870.63	0.97
Te $3p_{3/2}$	819.40	3.93
Te $3p_{1/2}$	870.20	3.93
Ni $2p_{3/2}$ Satellite	860.10	5.5
Ni $2p_{1/2}$ Satellite	877.32	4.5
Ni $2p_{3/2}$ Plasmon	872.78	6.0
Te $3p_{3/2}$ Plasmon	838.66	11.19
Te $3p_{1/2}$ +Ni $2p_{1/2}$ Plasmon	889.72	9.76

next higher BE main peak has a BE of 853.6 eV and corresponds to the Ni $2p_{3/2}$ peak. These values of Te $3p_{1/2}$ and Ni $2p_{3/2}$ are consistent with known BEs of metallic Te and Ni⁵⁴. Based on this information and the known spin-orbit (SO) doublet splittings of Ni $2p$ (~ 17.3 eV) and Te $3p$ (~ 51.0 eV) from reference data⁵⁴, we can expect the SO split Ni $2p_{1/2}$ peak at a BE of 870.9 eV, and the Te $3p_{1/2}$ peak at 870.4 eV. Thus the Ni $2p_{1/2}$ peak and the Te $3p_{1/2}$ peak are expected to be separated just by 0.5 eV, and hence, they essentially overlap each other. Further, as the HAXPES and SX-PES spectra have been normalized at the Te $3p_{3/2}$, it can be seen in Fig. 2(a) that the Ni $2p_{3/2}$ as well as the overlapping Ni $2p_{3/2}$ +Te $3p_{1/2}$ peaks show higher intensities compared to Te $3p_{3/2}$ peak in SX-PES compared to HAXPES. This is due to the fact that Ni $2p$ states have a higher photo-ionization cross-section (PICS) than Te $3p$ states for the photon energies used in SXPES compared to HAXPES⁵⁷. This observation suggests that the Ni $2p_{1/2}$ peak and the Te $3p_{1/2}$ peak overlap and we confirm it by carrying out a least-squares fitting using discussed below.

In order to characterize the details of the independent contributions of Ni $2p_{1/2}$ and Te $3p_{1/2}$ main peaks, as well as that of the weaker features, we carried out a least-squares fitting of the spectra, as shown in Fig. 2(b) and (c) for SXPES and HAXPES data, respectively. The fitting used SO splitting energies of 17.3 eV and 50.8 eV for Ni $2p$ and Te $3p$, respectively, consistent with reported values for metallic Ni and Te⁵⁴. The Te $3p_{3/2}$ and Te $3p_{1/2}$ shows broad satellites at $\approx 19.7 \pm 0.1$ eV, and similar features at ≈ 19.7 higher BEs are also seen in Te $3d$ spectra (Fig. 1), we assign them to plasmon excitations. For the fitting, we constrained the intensity ratios of Ni $2p_{3/2}$: Ni $2p_{1/2}$ and Te $3p_{3/2}$: Te $3p_{1/2}$ to the expected value of 2 : 1 and used asymmetric Doniach-Sunjic Voigt lineshapes for the main peaks and charge-transfer

satellites, and symmetric Gaussians for the plasmon features. However, since the Ni $2p_{3/2}$ main peak shows a satellite about 8 eV higher BE, it indicates the Ni $2p$ peaks also show a charge transfer(CT) satellite similar to other known Nickel compounds. Accordingly, just above the Ni $2p_{3/2}$, we used an asymmetric Voigt function for the CT satellite while just above the Ni $2p_{1/2}$ main peak, we included one Gaussian for the Ni $2p_{3/2}$ main peak plasmon and another asymmetric Voigt function for the weaker CT satellite. The total and component fits to the Ni $2p$ and Te $3p$ spectra for both SXPES and HAXPES are shown in Fig. 2(b) and (c), respectively, and the obtained BEs and their full-width and half-maximum (FWHM) are listed in Table II. The main peak BEs are very similar for Ni $2p$ and Te $3p$ core levels in both, SXPES and HAXPES data. In particular, the Ni $2p_{1/2}$ and Te $3p_{1/2}$ peak positions are quite close to each other ($0.5 \text{ eV} \pm 0.1 \text{ eV}$) as estimated from the BEs using Ni $2p_{3/2}$ and Te $3p_{3/2}$ BEs and the known SO splitting. The Ni $2p$ and Te $3p$ results are also consistent with a recent measurement⁵⁶) on NiTe₂. Further, the present Te $3p$ results indicate the main peak BEs and the plasmon energies are quite close to values reported by us for CoTe₂ measurements⁵⁵.

We then carried out Ni $2p$ - $3d$ resonant-PES of NiTe₂ to quantify the experimental value of U_{dd} from measurements of the single particle $3d$ partial density of states (PDOS) and the two hole correlation satellite using the Cini-Sawatzky method⁵⁸⁻⁶⁰. Fig. 3(a) shows the Ni $2p$ - $3d$ resonant PES valence band intensity map as a function of photon energies ($h\nu = 849\text{-}879$ eV) versus BE ($= -1.2$ to 45.8 eV). The resonant PES map is obtained by first measuring the Ni $L_{3,2}$ -edge XAS Fig. 3(b) as a function of $h\nu$ (top X-axis). Then, at different incident photon energies $a - \nu$ marked by arrows in the XAS spectrum(Fig. 3(b)), we measure the valence band spectra and plot the spectral intensity as the map shown in Fig. 3(a). Fig. 3(c) shows valence band spectra (BE = -1.2 eV to 35.0 eV) measured at select $h\nu$ values (labelled $a - \nu$) across the L_3 and L_2 edge of Fig. 3(b). The BEs are calibrated with respect to E_F of metallic NiTe₂ and the spectra are normalized to the shallow Te $4d_{5/2,3/2}$ core level peaks (bright blue vertical lines at ~ 40 and 42 eV BEs) in the map. The normalization shown in Fig. 3a and 3c at the Te $4d_{5/2}$ and $4d_{3/2}$ peaks is carried out to describe the resonance effects in the main Ni $3d$ states close to $h\nu = 853$ eV, and the evolution of the two-hole correlation satellite peak for $h\nu > 853$ eV, discussed below. Several well-resolved spectral features derived from Ni d bands and Te $5p$ bands are observed in the valence band spectra. The weak spectral feature at 1.90 eV BE shows a small increase in intensity when incident $h\nu$ values just cross the L_3 and L_2 edges and indicate a Ni $2p$ - $3d$ resonance of the Ni $3d$ derived partial density of states (PDOS) (green and yellow vertical line observed in Fig. 3(a) map, and yellow line also marked in Fig. 3(c)), consistent with low energy He I ARPES measurements of Ni $3d$ band⁶¹. The central feature in the Fig. 3(a) map is the diagonal from right bottom to left top. It originates in a feature at 7.90 eV BE in the map and Fig. 3(c), and shows a significantly large increase in intensity on increasing $h\nu$ from $a - e$, i.e., upto the Ni L_3 -edge maxima (blue vertical dotted line in the map and Fig. 3(c). On increasing $h\nu$ further from $f - l$, this

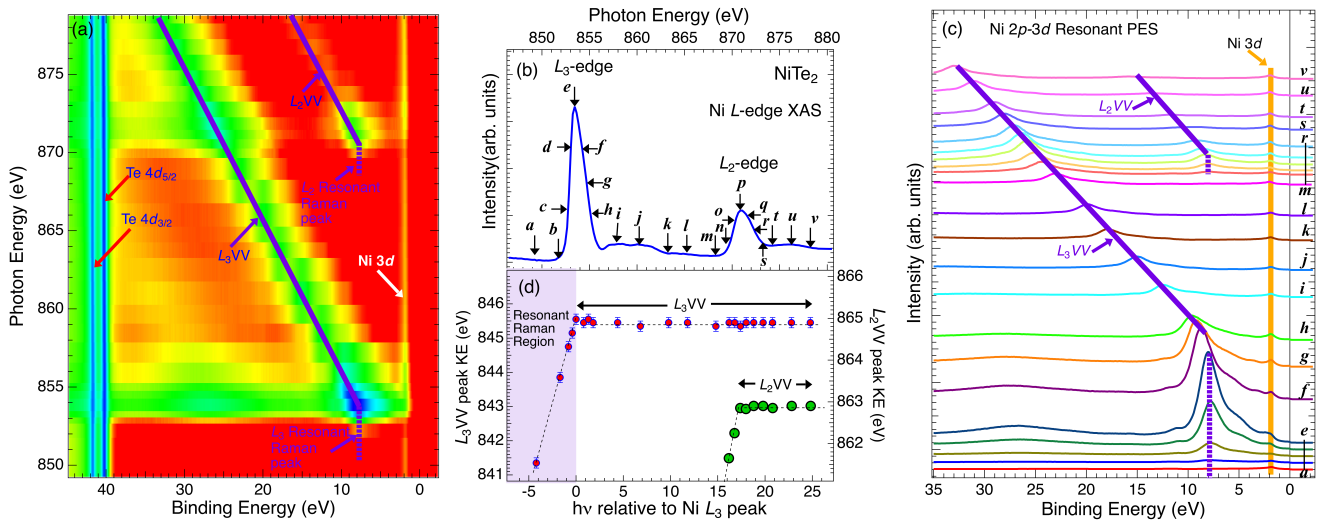


FIG. 3. (a). The Ni $2p$ - $3d$ resonant-PES valence band intensity map plotted as a function of incident photon energies ($h\nu = 849$ - 879 eV) versus BE ($= -1.2$ to 45.8 eV). (b) The Ni L_3 - and L_2 -edge XAS plotted as a function of $h\nu$ (top X-axis). (c) Valence band spectra (BE = -1.2 to 35.0 eV) measured at select $h\nu$ values (labelled $a - v$) across the L_3 - and L_2 -edges of Fig. 1(b). (d) The kinetic energy of the Resonant Raman peak which becomes the L_3VV Auger peak, plotted as a function of $h\nu$ relative to the XAS L_3 peak energy (bottom X-axis).

feature systematically moves to higher BEs with a shift equal to the increase in $h\nu$. This behavior of shift in BE equal to increase in $h\nu$ indicates its Ni L_3VV Auger feature (marked by the blue diagonal line in the map and in Fig. 3(c)). Fig. 3(d) shows a plot of the kinetic energy of this peak as a function of $h\nu$ relative to the XAS L_3 peak energy (bottom X-axis). The corresponding incident $h\nu$ values are the same as top X-axis of Fig. 3(b). This indicates that the ~ 7.90 eV constant BE feature for $h\nu = a - e$ represents a resonant Raman feature and it becomes a correlation satellite with two holes in the final state⁶²⁻⁶⁴. The map and Fig. 3(c) also shows a weak broad feature at ~ 19.3 eV BE for $h\nu$ across the Ni L_3 edge, which is attributed to a plasmon feature as seen in core level spectra. For higher $h\nu$ from $m - v$, the map and Fig. 3(c) again show a weak resonant Raman behavior (blue vertical dotted line), followed by the L_2VV two-hole correlation satellite Auger peak (blue full line) of the 7.90 eV BE feature. The corresponding kinetic energy of this peak as a function of $h\nu$ is also plotted in Fig. 3(d) and confirms its Auger character.

Figure 4 shows the valence band spectra measured at three different off-resonant photon energies of values $h\nu = 849.25$ eV, 1.5 keV, 6.5 keV, and one in the Resonant Raman region with $h\nu = 851.75$ eV. All these spectra are normalized at the broad spectral feature at 11.5 eV BE, which corresponds to the Te $5s$ shallow core level. The purpose of this normalization is to emphasize the relative spectral weights of Te $5p$ states and Ni $3d$ states. The normalization in Fig. 4 shows the intensities of the Ni $3d$ main band as well as the two-hole satellite at 7.9 eV BE relative to the intensity of the Te $5s$ states. It also identifies the Te $5p$ states in the $h\nu = 6.5$ keV HAXPES spectrum. Please note that for photon energy b , $h\nu = 851.75$ eV spectrum (blue curve), the photon energy is in the Resonant Raman region and the resonance effect is strong for ~ 8 eV BE, but weak for the main Ni $3d$ band at 1.9 eV BE, be-

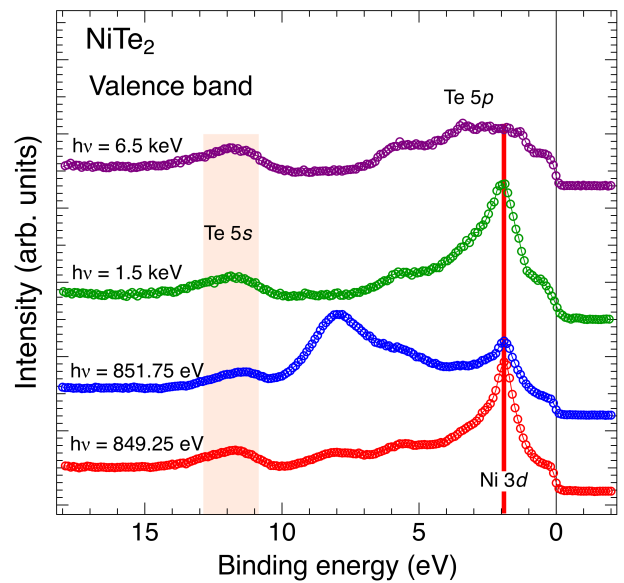


FIG. 4. NiTe₂ valence band measurements at different off-resonant $h\nu$ values of $h\nu = 849.25$ eV, 1.5 keV, 6.5 keV, and one in the Resonant Raman region with $h\nu = 851.75$ eV.

cause photon energy b , $h\nu = 851.75$ eV, is still below the main Ni L_3 peak energy (see Fig. 3b, 3d).

Comparison of the spectra obtained with the two lowest $h\nu$ values, indicates that the Ni $3d$ PDOS peak at 1.90 eV BE in Fig. 4 shows a weak suppression in the Resonant Raman region ($h\nu(b) = 851.75$ eV) but the two-hole satellite at 7.9 eV BE gets enhanced, when compared to the off-resonant ($h\nu(a) = 849.25$ eV) spectrum. However, the spectral shape recovers at higher energies from photon energy $h\nu(e) = 853$ eV (Figs.

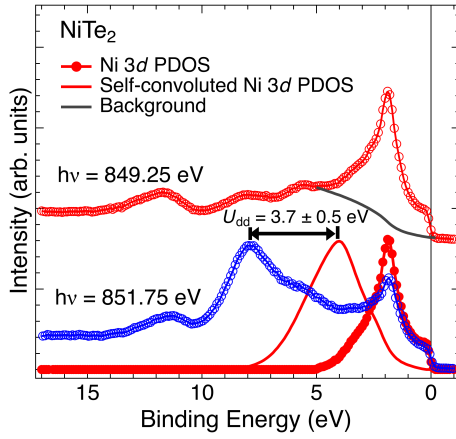


FIG. 5. The Ni 3d partial density of states (red color;●) are obtained by subtracting a Shirley-type integral background (black line) from off-resonance valence band spectrum obtained at $h\nu = 849.25$ eV (red color;○). Comparing the peak in the self-convolution of Ni 3d PDOS (red line) with the two-hole correlation satellite peak seen in the Resonant Raman region spectrum ($h\nu = 851.75$ eV; blue color ○), the average on-site Coulomb energy is estimated as the energy difference between the two peaks.

3a, 3c). The spectral shape for off-resonant $h\nu = 1.5$ keV is also fairly similar to off-resonant $h\nu = 849.25$ eV. On the other hand, at $h\nu = 6.5$ keV, the 1.90 eV BE and 7.9 eV BE features get strongly suppressed at $h\nu = 6.5$ keV due to the strongly reduced PICS of Ni 3d states compared to the Te 5p states at $h\nu = 6.5$ keV⁵⁷. At $h\nu = 6.5$ keV, the Te 5p states dominate the spectrum as the PICS ratio of Te 5p : Ni 3d is 6.41⁵⁷. This indicates that the feature at E_F corresponds to dominantly Te p PDOS. This is consistent with reported DFT electronic structure calculations and ARPES measurements which concluded that Te p states lie at E_F and within 0.5 eV BE^{39–42,44,65}. As we will show in Fig. 6 below, this observation is also consistent with a negative Δ in NiTe₂. Before that, we quantify U_{dd} using the Cini-Sawatzky method^{58–60} applied to the experimental Ni 3d PDOS and two-hole correlation satellite data.

Figure 5 shows the off resonance spectrum obtained with $h\nu = 849.25$ eV before/after (red ○/●) subtracting a Shirley-type integral background in order to separate out the single-particle Ni 3d PDOS from the Te 5p states at higher BEs. We have also tested for a linear background and the results showed hardly any change for the self-convoluted two-hole spectrum as well as the subsequent determination of U_{dd} . The single-particle PDOS was then numerically self-convoluted to obtain the two-hole spectrum (red line), and its peak energy represents the average two-hole energy without correlations. This two hole spectrum was then compared with the spectrum exhibiting the experimental two-hole correlation satellite spectrum in the resonant Raman region ($h\nu = 851.75$ eV; blue color ○). In the Cini-Sawatzky method, the energy difference between the peak in the two-hole spectrum without correlations and the peak of the experimental two-hole correlation satellite gives an estimate of the on-site Coulomb energy U_{dd} . We obtain the value of $U_{dd} = 3.7$ eV for Ni 3d states, indicating that

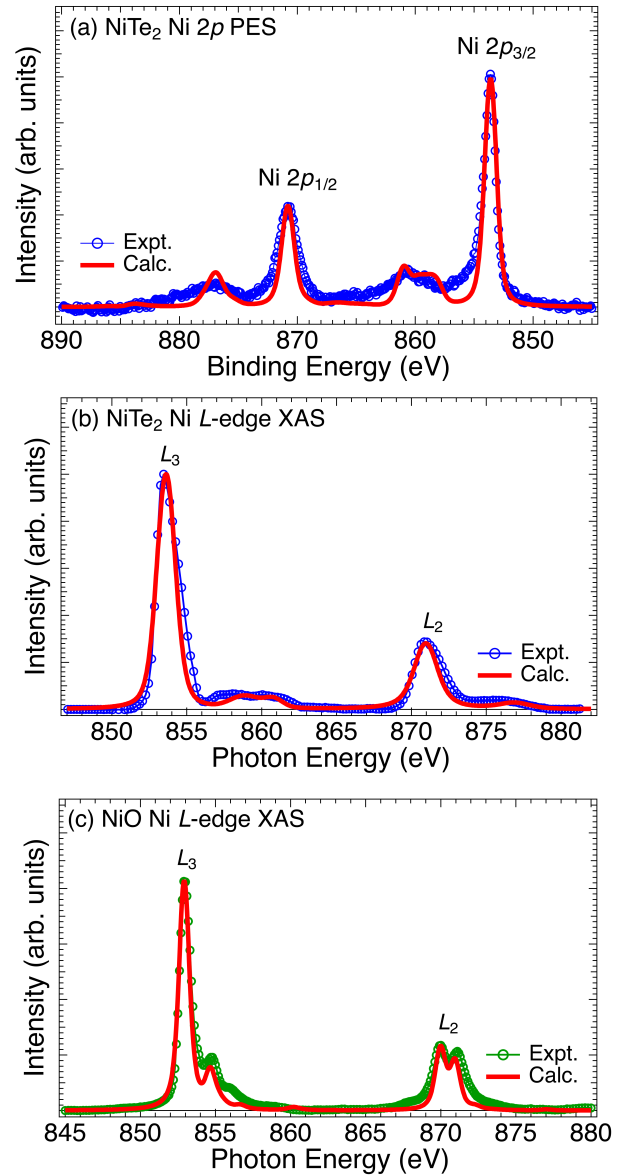


FIG. 6. (a) Ni 2p SXPS core level, (b) Ni $L_{3,2}$ -edge XAS of NiTe₂, and (c) Ni $L_{3,2}$ -edge XAS of NiO, compared with atomic multiplet charge transfer cluster model calculations.

the NiTe₂ is a moderately correlated metal. In the following, we use the obtained U_{dd} value in charge-transfer cluster model calculations to simulate the Ni 2p core-level PES and L-edge XAS spectra of NiTe₂ to independently check its validity.

Figures 6(a) and (b) show the experimental Ni 2p PES core level and Ni L-edge XAS spectra of NiTe₂ compared with charge transfer cluster model simulations obtained using $U_{dd} = 3.7$ eV and optimizing other electronic parameters. Due to the overlapping Ni 2p_{1/2} and Te 3p_{1/2} peaks, the experimental Ni 2p PES core level spectrum shown in Fig. 6(a) was obtained by subtracting out the fits to the Te 3p_{1/2} main peak and its plasmon, as well as the Ni 2p_{3/2} plasmon fit. For the Ni $L_{3,2}$ -edge XAS shown in Fig. 6(b), since the Te M₅-edge

TABLE III. Electronic parameters, spin magnetic moments m_S , and total d^n -counts for NiTe₂ and NiO using 3-basis state cluster model calculations.

Parameter	NiTe ₂	NiO
U_{dd} (eV)	3.7	7.0
Δ (eV)	-2.8	6.0
T_{eg} (eV)	1.8	2.4
T_{L2g} (eV)	0.9	1.2
$10Dq$ (eV)	0.5	1.65
F_k, G_k	1.0	0.8
m_S (μ_B)	0.96	1.82
d^n count	9.1	8.14

region did not show significant intensity in the XAS spectrum due to very low cross-section, we did not need to subtract a corresponding feature for the Te M₄-edge region. We confirmed that the spectral lineshape of Ni L_{3,2}-edge XAS shown in Fig. 6(b) is very similar to the reported Ni L_{3,2}-edge XAS of NiTe₂ single-crystal cleaved surface, including the satellite structures for the Ni L_{3,2}-edge⁵⁶. We then carried out an extensive set of calculations by varying Δ , T_{eg} , T_{L2g} ($=T_{eg}/2$) and $10Dq$ to optimize the parameters, as shown in Figs. 7 and 8 and discussed below. Using the experimental $U_{dd} = 3.7$ eV, and the same set of optimized parameters as listed in Table III, we could obtain calculated spectra close to the experiment for both Ni 2*p* PES and Ni L-edge XAS spectra as shown in Fig. 6(a) and (b), respectively. Similarly, using $U_{dd} = 7.0$ eV (from earlier XAS calculations for NiO; ref.^{66,67}), we optimized the other parameters for Ni L-edge XAS spectrum of NiO (as shown in Fig. 9 and described below). In Table III, we list the optimal values used to obtain the calculated spectra close to experiment shown in Fig. 6(a,b) for NiTe₂ and in Fig. 6(c) for NiO.

The comparison of electronic parameters for NiTe₂ and NiO, spin magnetic moments, and d^n counts in Table III indicates that NiTe₂ is a moderately correlated negative charge-transfer metal in the Zaanen-Sawatzky-Allen (ZSA) scheme⁴⁸, while NiO is a positive charge-transfer insulator as is well-known⁶⁶⁻⁷⁰. Further, we confirmed that the ground state of NiO consists of a mixture of 85.0% d^8 , 14.6% $d^9\bar{L}^1$ and a very small contribution of 0.4% $d^{10}\bar{L}^2$ weights. This is consistent with the early study of Fujimori and Minami which showed NiO has a ground state consisting of a mixture of 83.0% d^8 and 17.0% $d^9\bar{L}^1$ weights⁶⁸. Thus NiO shows a dominantly d^n character ground state. In contrast, the ground state of NiTe₂ consists of a mixture of 19.5% d^8 , 57.4% $d^9\bar{L}^1$ and a 23.1% $d^{10}\bar{L}^2$ weights. The negative- Δ for NiTe₂ also implies that E_F lies in the ligand states and the lowest energy excitations are $p \rightarrow p$ type excitations, consistent with ARPES results^{39-42,44,65}.

In Fig. 7(a) and (b), we plot a series of calculated Ni 2*p* PES and Ni L-edge XAS spectra, respectively, in order to check the optimal value of F_k and G_k for NiTe₂. By varying them together from a reduction factor of $R = 1.0$ to 0.1, keeping all other parameters fixed to the optimal values for NiTe₂, we confirm that for $R = 1.0$ i.e. no reduction of F_k and G_k results in the least deviation compared to experiment.

In Fig. 8(a) and (b), we plot a series of calculated Ni 2*p* PES

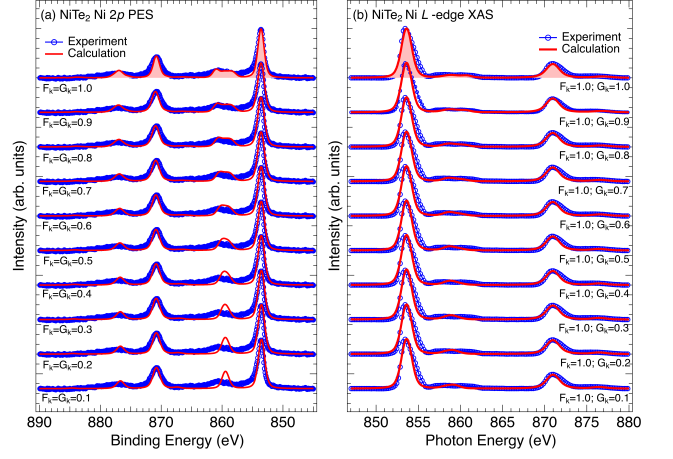


FIG. 7. Optimization of F_k and G_k for (a) Ni 2*p* PES and (b) Ni L-edge XAS of NiTe₂

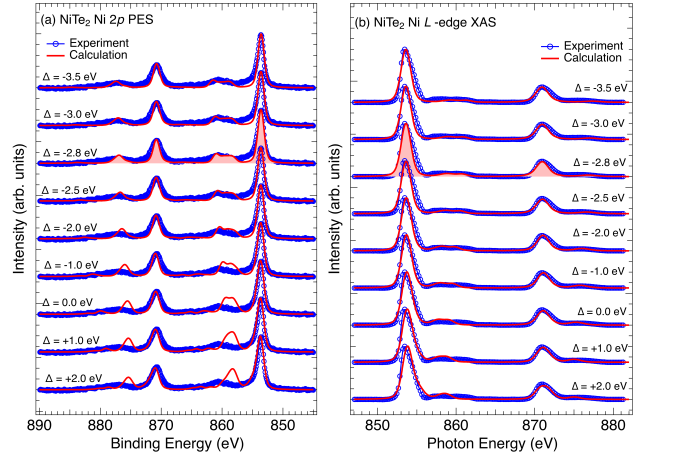


FIG. 8. Optimization of charge transfer energy Δ for (a) Ni 2*p* PES and (b) Ni L-edge XAS of NiTe₂

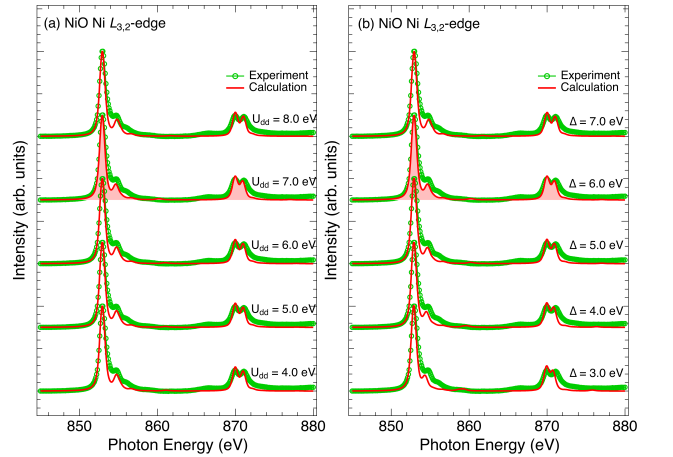


FIG. 9. (a) Optimization of on-site Coulomb energy U_{dd} and (b) charge transfer energy Δ for Ni L_{3,2}-edge XAS of NiO

and Ni L -edge XAS spectra, respectively, to check the optimal value of charge transfer energy Δ for NiTe₂. By varying it from $\Delta = -3.5$ eV to $+2.0$ eV, and keeping all other parameters fixed to the optimal values, it is confirmed that the Ni $2p_{3/2}$ and Ni $2p_{1/2}$ PES satellites to the main peaks as well as the Ni L -edge XAS satellites show the least deviation compared to the experiment for $\Delta = -2.8$ eV.

Figure 9 (a) and (b) shows a series of calculated Ni $L_{3,2}$ -edge XAS spectra for checking the the optimal value of on-site Coulomb energy U_{dd} and charge transfer energy Δ for NiO, respectively. U_{dd} is varied from 4.0 eV to 8.0 eV, in 1.0 eV steps, by keeping all other parameter fixed (Fig. 10 (a)) and Δ is varied from 3.0 eV to 7.0 eV, in 1.0 eV steps, by keeping all other parameters fixed (Fig. 10 (b)). The results confirm that the least deviation between calculated and experimental spectra is obtained for $U_{dd} = 7.0$ eV and $\Delta = 6.0$ eV.

In order to understand the evolution from an effective positive- Δ to negative- Δ , we carried out a set of CT cluster model calculations to investigate the relation of Δ and U_{dd} with d^n . In Fig. 10, we plot the variation of d^n count vs. T_{eg} for different Δ values (red curves), and all other parameters were fixed to optimal values of NiTe₂. The curves show that for Ni²⁺, starting with $d^n = 8$ for $T_{eg} = 0$, a sharp increase of ~ 1 electron to $d^n \sim 9$ is obtained for a finite $T_{eg} = 5$ meV, for values of negative $\Delta \leq \Delta_C = -1.55$ eV. This is attributed to a spontaneous charge transfer which causes an effective negative- Δ to form the dominantly $3d^{n+1}\bar{L}^1$ ground state even for a small $T_{eg} = 5$ meV. In region A of Fig. 10, it is seen that using optimal parameters ($\Delta = -2.8$ eV and $T_{eg} = 1.8$ eV) corresponding to spectra shown in Figs. 6(a,b), we obtain $d^n = 9.1$ (black square in red curve for $\Delta = -2.8$ eV). Fig. 10 also shows the variation of d^n count vs. T_{eg} for $U_{dd} = 3.0$ to 6.0 eV (green curves; all other parameters fixed to optimal values of NiTe₂). The region A (pink shade) in Fig. 10 shows that an increase in d^n is obtained on reducing Δ (making it more negative; red arrow) or reducing U_{dd} (green arrow). This indicates that a large CT from ligand to Ni site in NiTe₂ is obtained from a combination of effective negative- $\Delta \leq \Delta_C$ and reduced U_{dd} . The reduction of U_{dd} is attributed to the larger polarizability of Te compared to oxygen anions, as polarizability is roughly proportional to the anion size⁷¹. Also, for $\Delta > \Delta_C$ i.e. Δ is more positive than Δ_C (region B; purple shade), the sharp jump in d^n for $T_{eg} = 5$ meV gets suppressed and instead shows a gradual rise as a function of T_{eg} .

Since it is somewhat surprising that the negative- Δ region occurs only for $\Delta < \Delta_C = -1.55$ eV in Fig. 10, we checked the relation of spin magnetic moments with Δ , and also calculated a series of XAS spectra for various Δ values across $\Delta_C = -1.55$ eV. Figure 11(a), shows the spin magnetic moment m_S vs. Δ for $T_{eg} = 5$ meV obtained from the same cluster model calculation results shown in Fig. 10, with all other parameters fixed to NiTe₂ optimal parameters. The m_S values exhibit a jump at $\Delta = -1.55$ eV, where even the total d^n count shows a jump in Fig. 10, and we denoted this value as Δ_C . The m_S values show negligible change for $\Delta \leq \Delta_C$, and also for $\Delta > \Delta_C$. However, the m_S vs. Δ curve for the optimal value of $T_{eg} = 1.2$ eV for NiTe₂, m_S shows a small gradual increase on increasing Δ . The corresponding individual ground state weights from

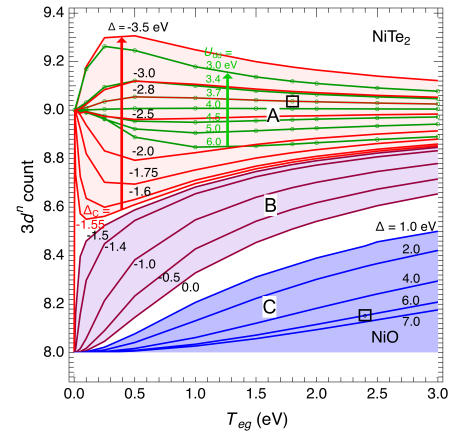


FIG. 10. Variation d^n -count vs. T_{eg} for selected values of Δ and U_{dd} of NiTe₂ and NiO. Region A corresponds to effective negative- Δ , and regions B and C correspond of effective positive- Δ . Squares(\square) indicate optimal values which reproduce experimental spectra shown in Fig. 6.

TABLE IV. Ground state weights (%) obtained from cluster model calculations with $T_{eg} = 5$ meV, starting with the formal d^8 configuration for NiTe₂

NiTe ₂	d^8	$d^9\bar{L}^1$	$d^{10}\bar{L}^2$
$\Delta = \Delta_C = -1.55$ eV (and all $\Delta < \Delta_C$)	10.3%	89.7%	0.0%
$\Delta = -1.5$ eV (and all Δ more +ve than Δ_C)	95.8%	0.42%	0.0%

the cluster model calculations for $T_{eg} = 5$ meV are listed in Table IV. It is clear from Fig. 10 and Table IV that for $\Delta \leq \Delta_C$, the results indicate a dominantly $d^{n+1}\bar{L}^1$ state corresponds to the effective negative- Δ region A of Fig. 10, and for $\Delta > \Delta_C$, it indicates a dominantly d^n state and corresponds to the effective positive- Δ region B of Fig. 10.

Similarly, for NiO, the spin magnetic moment m_S vs. Δ for $T_{eg} = 5$ meV are plotted in Fig. 11(b). These are also obtained from the calculation results of NiO shown in Fig. 10 (region C; blue curves; blue shade). The NiO results show that the d^n count starts from $d^n = 8$ for $T_{eg} = 0$, and shows a small gradual increase on increasing T_{eg} . Further, as a function of Δ , the

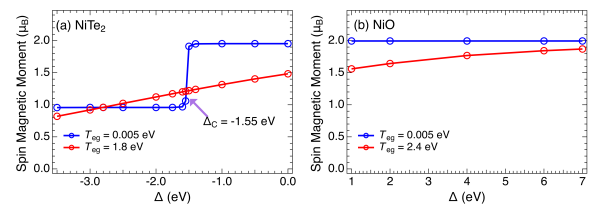


FIG. 11. (a) In NiTe₂, the spin magnetic moment m_S vs. Δ for $T_{eg} = 5$ meV, exhibits a jump at $\Delta_C = -1.55$ eV, while for optimal $T_{eg} = 1.8$ eV, m_S vs. Δ shows a gradual change across Δ_C . (b) In NiO, the m_S vs. Δ shows a nearly constant value for small $T_{eg} = 5$ meV, while for optimal $T_{eg} = 2.5$ eV, m_S vs. Δ shows a gradual change with Δ .

the d^n count shows a systematic decrease on increasing Δ for fixed T_{eg} values. The m_S values vs. Δ for $T_{eg} = 5$ meV show a negligible change for all Δ values, while the m_S vs. Δ curve for the optimal value of $T_{eg} = 2.4$ eV shows a small gradual increase of m_S on increasing Δ . These results indicate that region C of Fig. 10 corresponds to the positive- Δ region, with qualitatively similar curves as in region B. In particular, for optimal parameters of NiO ($\Delta = 6.0$ eV and $T_{eg} = 2.4$ eV) corresponding to spectra shown in Fig. 6(c), the obtained value of $d^n = 9.1$ (black square in blue curve for $\Delta = 6.0$ eV in region C of Fig. 10). Further, the m_S values on increasing Δ in Fig. 11(a) connect to the m_S values on increasing Δ in Fig. 11(b), thus confirming that region B is an effective positive- Δ region.

The above observations are qualitatively similar to the behavior of spin magnetic moments m_S vs. Δ in CoTe₂. In order to answer the question about why $\Delta_C = -1.55$ eV in NiTe₂, we follow the case of CoTe₂, for which we have recently reported⁵⁵ that regions A and B are separated across $\Delta_C = 0.3$ eV. It was found that the true negative- Δ region is obtained when the charge transfer energy is defined as the energy difference between the energies of the lowest multiplet of $d^{n+1}\underline{L}^1$ and d^n configurations⁷²⁻⁷⁴, and not in terms of the difference between the average energy of the d^n multiplets and the average energy of $d^{n+1}\underline{L}^1$ multiplets.

Accordingly, we then checked at what value does the ground state transform from a dominantly d^n state to $d^{n+1}\underline{L}^1$ state i.e. negative Δ represents $\Delta < 0$ or $\Delta_{eff} < 0$ for NiTe₂. In cluster model calculations, Δ is usually defined as, $\Delta = E(d^{n+1}\underline{L}^1) - E(d^n)$, where $E(d^n)$ is the average energy of the d^n multiplets and $E(d^{n+1}\underline{L}^1)$ is the average energy of $d^{n+1}\underline{L}^1$ multiplets. On the other hand, if the energy difference of the lowest multiplet and the average multiplet energy is $\Delta'E_n$, then the effective charge transfer energy is $\Delta_{eff} = \Delta + \Delta'E_{n+1} - \Delta'E_n$. We calculated L -edge XAS spectra with a small $T_{eg} = 5$ meV for various Δ values at and across Δ_C , with a very small Gaussian broadening of 0.1 eV FWHM as shown in Fig. 12. The L -edge XAS spectrum corresponds to transitions from the ground state to final states of the type $2p^63d^n \rightarrow 2p^53d^{n+1}$, $2p^63d^{n+1}\underline{L}^1 \rightarrow 2p^53d^{n+2}\underline{L}^1$, etc. The obtained results shown in Fig. 12 show that the actual transition to a negative charge-transfer character takes place when $\Delta_{eff} < 0$, and not for $\Delta < 0$, as described in the following.

Fig. 12(a-c) shows the L -edge XAS spectra with a small $T_{eg} = 5$ meV and a small Gaussian broadening of 0.1 eV FWHM for selected Δ values, with all other parameters fixed to optimal values of NiTe₂. The spectra in panel(a) for $\Delta \leq \Delta_C = -1.55$ eV show hardly any change in the shape of the multiplet features but show a systematic shift equal to the change in Δ . From Table IV, it is clear that all the spectra originate in the dominantly $d^{n+1}\underline{L}^1$ initial state multiplets. In panel (b), we plot four spectra for $\Delta > \Delta_C = -1.55$ eV (i.e. Δ more positive than Δ_C) and the results show very similar spectra but with significantly different multiplet features. From Table IV, we know that for $\Delta = 1.5$ eV, the initial state is dominated by the d^n state. This indicates the spectra in panel (b) originate in the d^n state and do not show a shift as is seen in Fig. 12(a) for $\Delta \leq \Delta_C$. In panel(c), we compare the spectra for $\Delta_C = -1.55$ eV with $\Delta = -1.5$ eV. We also plot the spectrum of $\Delta = -1.55$

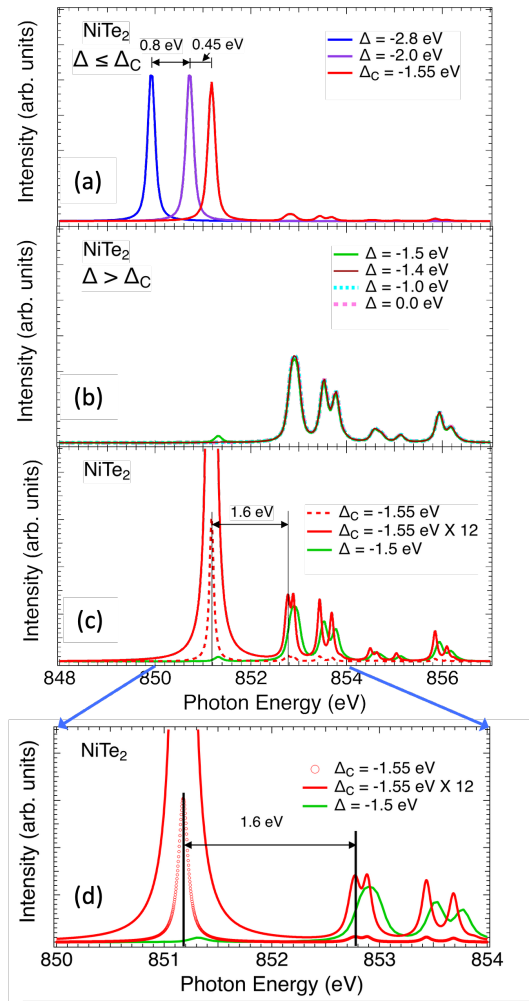


FIG. 12. The XAS spectral calculations for $T_{eg} = 5$ meV and varying Δ with all other parameters fixed to optimal values of NiTe₂: (a) for $\Delta \leq \Delta_C = -1.55$ eV, (b) for $\Delta > \Delta_C = -1.55$ eV (c) for $\Delta = \Delta_C = -1.55$ eV ($d^{n+1}\underline{L}^1$ state) and $\Delta = -1.5$ eV (d^n state) (d) same as (c), but plotted on an expanded x-scale.

eV calculated with a smaller 0.01 eV FWHM Gaussian broadening to see fine features. Panel (d) shows the same spectra plotted on an expanded x-scale. The lowest energy multiplet of the $\Delta_C = -1.55$ eV spectrum is shifted by 1.6 ± 0.1 eV compared to the dominant energy multiplet of the $\Delta = -1.5$ eV spectrum. This difference of the spectral behavior for $\Delta \leq \Delta_C$ and $\Delta > \Delta_C$, together with the results of d^n count of Fig. 10 indicate that region A with $\Delta \leq \Delta_C = -1.55$ eV corresponds to the effective negative- Δ region, and region B with $\Delta > \Delta_C$ corresponds to an effective positive- Δ region.

We have thus confirmed that Δ_C for NiTe₂ corresponds to attaining an effective negative Δ , defined as the energy difference between lowest multiplet of d^n and $d^{n+1}\underline{L}^1$ states⁷²⁻⁷⁴, i.e. a material attains a genuine negative- Δ state for $\Delta \leq \Delta_C$, when the lowest multiplet of the $d^{n+1}\underline{L}^1$ state becomes more negative than lowest multiplet of the d^n state. Fig. 10 highlights regions of effective negative- Δ (A) and effective positive- Δ (B, C). A similar detailed analysis of the relation of d^n with Δ

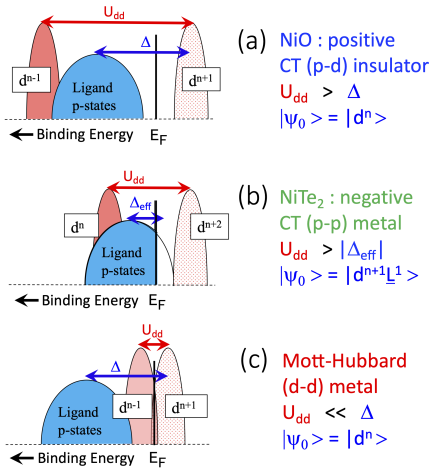


FIG. 13. Schematic electronic structure of: (a) NiO: a positive- Δ charge-transfer insulator with $U_{dd} > \Delta$ and $p \rightarrow d$ type lowest energy excitations (b) NiTe₂: an effective negative- Δ metal with a reduced U_{dd} , but with $U_{dd} > |\Delta_{eff}|$ and E_F is within the ligand- p band states, facilitating band inversion with $p \rightarrow p$ type lowest energy excitations to make it a correlated topological metal. (c) a Mott-Hubbard metal with $U_{dd} \ll \Delta$. A slightly larger U_{dd} but still less than Δ would result in a Mott-Hubbard insulator if the lower(occupied) and upper(unoccupied) Hubbard d -bands have a band gap. For Mott-Hubbard and positive- Δ materials, the ground state $|\psi_0\rangle$ has dominantly $|d^n\rangle$ character, while for negative- Δ materials, $|\psi_0\rangle$ has dominantly $|d^{n+1}\underline{L}^1\rangle$ character, where \underline{L}^1 is a ligand p -band hole.

U_{dd} in CoTe₂ using CT cluster model calculations is reported in ref.⁵⁵.

Figure 13(a) shows the schematic electronic structure of NiO with $U_{dd} > \Delta$. It is noted that while the NiO Ni L -edge XAS can be reproduced fairly with a single metal site cluster model calculation^{66,67}, the Ni 2p core level PES was shown to require a multiple Ni-site calculation⁶⁹, or a single metal-site CT multiplet calculation combined with DMFT calculations⁷⁰, to reproduce the additional well-screened peak observed in 2p PES arising from non-local screening. Fig. 13(b) shows the schematic electronic structure of NiTe₂ with a reduced U_{dd} compared to NiO, but still $U_{dd} > |\Delta|$ with a dominantly $d^{n+1}\underline{L}^1$ contribution in the ground state.

The obtained values of d - p hybridization strength T_{eg} indicate that T_{eg} is smaller for NiTe₂ compared to NiO, consistent with Ni-Te distance ($= 2.620\text{\AA}$) being larger than Ni-O distance ($= 2.09\text{\AA}$). This indicates that the reduced U_{dd} in NiTe₂ compared to NiO is not due to an increase in T_{eg} . The large increase in d^n count on the Ni site ($d^n = 9.1$) by more than one electron compared to a formal $d^n = 8$ for divalent NiTe₂ is attributed to negative- Δ and a reduced U_{dd} . While the value of U_{dd} in NiTe₂ gets reduced by nearly 50% compared to NiO, the moderately repulsive value of $U_{dd} = 3.7$ eV is crucial to achieve topological properties in NiTe₂ as follows: if U_{dd} was $\ll |\Delta|$, NiTe₂ would exhibit a Mott-Hubbard metal character with $d \rightarrow d$ type lowest energy excitations (Fig. 13(c)) in the

ZSA phase diagram⁴⁸. This would imply weak spin-orbit coupled $3d$ states in the vicinity of E_F and absence of band inversion. Accordingly, NiTe₂ would not be a topological Dirac semi-metal. Thus, only because $U_{dd} > |\Delta|$, the $3d$ states are pushed away from E_F and NiTe₂ becomes a topological Dirac semi-metal with band inversion and $p \rightarrow p$ type excitations between strongly spin-orbit coupled Te $5p$ derived states. The results then show that the present approach, based on quantifying the value of U_{dd} using the Cini-Sawatzky method from experimental single particle DOS and the two hole satellite energy provides a valid estimate of U_{dd} . Having employed this value in cluster model calculations to obtain theoretically simulated spectra which are close to the experimental spectra, we obtain the additional parameters of a negative charge transfer energy Δ and T_{eg} for NiTe₂. From this exercise, our results show that a finite U_{dd} is indeed necessary to explain the electronic structure of NiTe₂ (moderately correlated negative- Δ), as well as its comparison with NiO (strongly correlated positive- Δ) in the ZSA phase diagram, and provides a more complete picture compared to earlier work.

IV. CONCLUSIONS

In conclusion, the core-level and valence band electronic structure of single crystal NiTe₂ was investigated for quantifying electronic parameters in NiTe₂. Using the Cini-Sawatzky method, we obtain a value of $U_{dd} = 3.7$ eV. The Ni 2p core level and L -edge XAS spectra were analyzed by charge transfer cluster model calculations using the obtained U_{dd} ($= 3.7$ eV), and the results indicate NiTe₂ is a negative charge-transfer material with $\Delta = -2.8$ eV. The same type of cluster model analysis for NiO L -edge XAS confirms its well-known strongly correlated charge-transfer insulator character, with $U_{dd} = 7.0$ eV and $\Delta = 6.0$ eV. The hybridization strength T_{eg} between Ni $3d$ and ligand states for NiTe₂ < NiO, and indicates that the reduced U_{dd} in NiTe₂ compared to NiO is not due to an increase in T_{eg} . The d^n count on the Ni site increases by nearly one electron in NiTe₂ due to negative- Δ and a reduced U_{dd} . Since $U_{dd} > |\Delta|$, the results indicate the important requirement of a finite repulsive U_{dd} in making NiTe₂ a moderately correlated p -type Dirac semi-metal.

ACKNOWLEDGMENTS

This work was supported by the National Science and Technology Council(NSTC) of Taiwan under Grant Nos. NSTC 113-2112-M-006-009-MY2 (CNK), 110-2124-M-006-006-MY3 (CSL), 112-2124-M-006-009 (CSL), 113-2112-M-007-033 (AF), 112-2112-M-213-029(AC) and 114-2112-M-213-021(AC). AF acknowledges support from the Yushan Fellow Program under the Ministry of Education of Taiwan and Grant No. JP22K03535 from Japan Society for the Promotion of Science(JSPS). ARS thanks the National Science and Technology Council(NSTC) of Taiwan for a post-doctoral fellowship under Grant No. NSTC 114-2811-M-213-006.

- ¹ S. Murakami, N. Nagaosa, N. and S.-C. Zhang, Spin-Hall insulator, *Phys. Rev. Lett.* 93, 156804 (2004).
- ² C. L. Kane and E. J. Mele, Z_2 topological order and the quantum spin Hall effect, *Phys. Rev. Lett.* 95, 146802 (2005).
- ³ B. A. Bernevig, T. L. Hughes and S.-C. Zhang, Quantum spin Hall effect and topological phase transition in HgTe quantum wells, *Science* 314, 1757-1761 (2006).
- ⁴ C. L. Kane and E. J. Mele, Topological insulators in three dimensions, *Phys. Rev. Lett.* 98, 106803 (2007).
- ⁵ J. E. Moore and L. Balents, Topological invariants of time-reversal-invariant band structures, *Phys. Rev. B* 75, 121306(R) (2007).
- ⁶ R. Roy, Topological phases and the quantum spin Hall effect in three dimensions, *Phys. Rev. B* 79, 195322 (2009).
- ⁷ H. Zhang, C. -X. Liu, X. -L. Qi, X. Dai, Z. Fang and S. -C. Zhang, Topological insulators in Bi_2Se_3 , Bi_2Te_3 and Sb_2Te_3 with a single Dirac cone on the surface, *Nat. Phys.* 5, 438 (2009).
- ⁸ M. König, S. Wiedmann, C. Brüne, A. Roth, H. Buhmann, L. W. Molenkamp, X.-L. Qi, and S.-C. Zhang, Quantum spin Hall insulator state in HgTe quantum wells, *Science* 318, 766 (2007)
- ⁹ D. Hsieh, D. Qian, L. Wray, Y. Xia, Y. S. Hor, R. J. Cava and M. Z. Hasan, A topological Dirac insulator in a quantum spin Hall phase. *Nature* 452, 970-974 (2008).
- ¹⁰ B. A. Volkov and O. A. Pankratov, Two-dimensional massless electrons in an inverted contact, *JETP Lett.* 42, 178(1985).
- ¹¹ O. A. Pankratov, S.V. Pakhomov and B.A. Volkov, Supersymmetry in heterojunctions: Band-inverting contact on the basis of $\text{Pb}_{1-x}\text{SnTe}$ and $\text{Hg}_{1-x}\text{CdTe}$, *Solid State Commun.* 61, 93-96 (1987)
- ¹² Y. Xia, D. Qian, D. Hsieh, L. Wray, A. Pal, H. Lin, A. Bansil, D. Grauer, Y. S. Hor, R. J. Cava and M. Z. Hasan, Observation of a large-gap topological-insulator class with a single Dirac cone on the surface, *Nat. Phys.* 5, 398–402 (2009).
- ¹³ Y. L. Chen, J. G. Analytis, J.-H. Chu, Z. K. Liu, S. -K. Mo, X. L. Qi, H. J. Zhang, D. H. Lu, X. Dai, Z. Fang, S. C. Zhang, I. R. Fisher, Z. Hussain, Z. -X. Shen, Experimental realization of a three-dimensional topological insulator, Bi_2Te_3 , *Science* 325, 178 (2009).
- ¹⁴ D. Hsieh, Y. Xia, D. Qian, L. Wray, F. Meier, J. H. Dil, J. Osterwalder, L. Patthey, A. V. Fedorov, H. Lin, A. Bansil, D. Grauer, Y. S. Hor, R. J. Cava, and M. Z. Hasan, Observation of time-reversal-protected single-Dirac-cone topological-insulator states in Bi_2Te_3 and Sb_2Te_3 , *Phys. Rev. Lett.* 103, 146401(2009).
- ¹⁵ A. A. Burkov and L. Balents, Weyl semimetal in a topological insulator multilayer, *Phys. Rev. Lett.* 107, 127205 (2011).
- ¹⁶ A. B. Sushkov, J. B. Hofmann, G. S. Jenkins, J. Ishikawa, S. Nakatsuji, S. Das Sarma, and H. D. Drew, Optical evidence for a Weyl semimetal state in pyrochlore $\text{Eu}_2\text{Ir}_2\text{O}_7$, *Phys. Rev. B* 92, 241108(R) (2015).
- ¹⁷ B. Q. Lv, H. M. Weng, B. B. Fu, X. P. Wang, H. Miao, J. Ma, P. Richard, X. C. Huang, L. X. Zhao, G. F. Chen, Z. Fang, X. Dai, T. Qian, and H. Ding, Experimental discovery of Weyl semimetal TaAs, *Phys. Rev. X* 5, 031013 (2015).
- ¹⁸ S. -M. Huang, S. -Y. Xu, I. Belopolski, C. -C. Lee, G. Chang, B. Wang, N. Alidoust, G. Bian, M. Neupane, C. Zhang, S. Jia, A. Bansil, H. Lin, and M. Z. Hasan, A Weyl Fermion semimetal with surface Fermi arcs in the transition metal monpnictide TaAs class, *Nat. Commun.* 6, 7373 (2015).
- ¹⁹ S. Souma, Z. Wang, H. Kotaka, T. Sato, K. Nakayama, Y. Tanaka, H. Kimizuka, T. Takahashi, K. Yamauchi, T. Oguchi, K. Segawa, and Y. Ando, Direct observation of nonequivalent Fermi-arc states of opposite surfaces in the noncentrosymmetric Weyl semimetal NbP, *Phys. Rev. B* 93, 161112(R) (2016).
- ²⁰ A. A. Zyuzin, Si Wu, and A. A. Burkov, Weyl semimetal with broken time reversal and inversion symmetries, *Phys. Rev. B* 85, 165110 (2012).
- ²¹ A. A. Burkov, Topological semimetals, *Nat. Mater.* 15, 1145 (2016).
- ²² M. S. Bahramy, O. J. Clark, B.-J. Yang, J. Feng, L. Bawden, J.M.Riley, I.Markovic, F.Mazzola, V.Sunko, D.Biswas, S. P. Cooil, M. Jorge, J. W. Wells, M. Leandersson, T. Balasubramanian, J. Fujii, I. Vobornik, J. E. Rault, T. K. Kim, M. Hoesch, K. Okawa, M. Asakawa, T. Sasagawa, T. Eknapakul, W. Meevasana, and P. D. C. King, Ubiquitous formation of bulk Dirac cones and topological surface states from a single orbital manifold in transition-metal dichalcogenides, *Nature Mater.* 17, 21 (2018).
- ²³ J. Shi, Y. Huan, M. Xiao, M. Hong, X. Zhao, Y. Gao, F. Cui, P. Yang, S. J. Pennycook, J. Zhao, and Y. Zhang, Two-Dimensional Metallic NiTe_2 with Ultrahigh Environmental Stability, Conductivity, and Electrocatalytic Activity, *ACS Nano* 14, 9011 (2020).
- ²⁴ Q. Mao, Y. Zhang, Q. Chen, R. Li, X. Geng, J. Yang, H. Hao, M. Fang, Metallicity and Paramagnetism of Single-Crystalline NiTe and NiTe_2 *Phys. Stat. Solidi B* 257, 1000224 (2020).
- ²⁵ Z. Feng, J. Si, T. Li, H. Dong, C. Xu, J. Yang, Z. Zhang, K. Wang, H. Wu, Q. Hou, J. -J. Xing, S. Wan, S. Li, W. Deng, J. Feng, A. Pal, F. Chen, S. Hu, J.-Y. Ge, C. Dong, N. -C. Yeh, Evidences for pressure-induced two-phase superconductivity and mixed structures of NiTe_2 and NiTe in type-II Dirac semimetal NiTe_{2-x} ($x = 0.38 \pm 0.09$) single crystals, *Mater. Today Phys.* 17, 100339 (2021).
- ²⁶ B. Pal, A. Chakraborty, P. K. Sivakumar, M. Davydova, A. K. Gopi, A. K. Pandeya, J. A. Krieger, Y. Zhang, M. Date, S. Ju, N. Yuan, N. B. M. Schroter, L. Fu and S. S. P. Parkin, Josephson diode effect from Cooper pair momentum in a topological semimetal, *Nature Phys.* 18, 1228 (2022).
- ²⁷ J. Oh, H. J. Park, A. Bala, H.-S. Kim, N. Liu, S. Choo, M. H. Lee, S. J. Kim, and S. Kim, Nickel telluride vertically aligned thin film by radio-frequency magnetron sputtering for hydrogen evolution reaction, *APL Mater.* 8, 121104 (2020).
- ²⁸ C. He, J.-Z. Zhao, M. Du, L.-Z. Zhang, J.-Y. Zhang, K. Yang, N. F. Q. Yuan, A. Seliverstov, E. Janssens, J.-Y. Ge, and Z. Li, Coexistence of topological surface states and superconductivity in Dirac semimetal NiTe_2 . (accepted in *Phys. Rev. Lett.*); DOI: <https://doi.org/10.1103/vpl7-n6bp>, cond-mat arXiv:2503.01337.
- ²⁹ Z. K. Liu, B. Zhou, Y. Zhang, Z. J. Wang, H. M. Weng, D. Prabhakaran, S.-K. Mo, Z. X. Shen, Z. Fang, X. Dai, Z. Hussain, and Y. L. Chen, Discovery of a three-dimensional topological Dirac semimetal, Na_3Bi , *Science* 343, 864 (2014).
- ³⁰ S.-Y. Xu, C. Liu, S. K. Kushwaha, R. Sankar, J. W. Krizan, I. Belopolski, M. Neupane, G. Bian, N. Alidoust, T.-R. Chang, H.-T. Jeng, C.-Y. Huang, W.-F. Tsai, H. Lin, P. P. Shibayev, F.-C. Chou, R. J. Cava, and M. Z. Hasan, Observation of Fermi arc surface states in a topological metal, *Science* 347, 294 (2015).
- ³¹ M. Neupane, S.-Y. Xu, R. Sankar, N. Alidoust, G. Bian, C. Liu, I. Belopolski, T.-R. Chang, H.-T. Jeng, H. Lin, A. Bansil, F. Chou, and M. Z. Hasan, Observation of a three-dimensional topological Dirac semimetal phase in high-mobility Cd_3As_2 , *Nat. Commun.* 5, 3786 (2014).
- ³² S. Borisenko, Q. Gibson, D. Evtushinsky, V. Zabolotnyy, B. Büchner, and R. J. Cava, Experimental realization of a three-dimensional Dirac semimetal, *Phys. Rev. Lett.* 113, 027603 (2014).

- ³³ K. Zhang, M. Yan, H. Zhang, H. Huang, M. Arita, Z. Sun, W. Duan, Y. Wu, and S. Zhou, Experimental evidence for Type-II Dirac semimetal in PtSe₂, *Phys. Rev. B* 96, 125102 (2017).
- ³⁴ H.-J. Noh, J. Jeong, E.-J. Cho, K. Kim, B. I. Min, and B.-G. Park, Experimental realization of type-II Dirac fermions in a PdTe₂ superconductor, *Phys. Rev. Lett.* 119, 016401 (2017).
- ³⁵ M. Yan, H. Huang, K. Zhang, E. Wang, W. Yao, K. Deng, G. Wan, H. Zhang, M. Arita, H. Yang, Z. Sun, H. Yao, Y. Wu, S. Fan, W. Duan, and S. Zhou, Lorentz-violating Type-II Dirac fermions in transition metal dichalcogenide PtTe₂, *Nat. Comm.* 8, 257 (2017).
- ³⁶ O. J. Clark, M. J. Neat, K. Okawa, L. Bawden, I. Markovic, F. Mazzola, J. Feng, V. Sunko, J. M. Riley, W. Meevasana, J. Fujii, I. Vobornik, T. K. Kim, M. Hoesch, T. Sasagawa, P. Wahl, M. S. Bahrany, and P. D. C. King, Fermiology and superconductivity of topological surface states in PdTe₂, *Phys. Rev. Lett.* 120, 156401 (2018).
- ³⁷ A. Chakraborty, J. Fujii, C.-N. Kuo, C. S. Lue, A. Politano, I. Vobornik, and A. Agarwal, Observation of highly anisotropic bulk dispersion and spin-polarized topological surface states in CoTe₂, *Phys. Rev. B* 107, 085406 (2023).
- ³⁸ C. Xu, B. Li, W. Jiao, W. Zhou, B. Qian, R. Sankar, N. D. Zhigadlo, Y. Qi, D. Qian, F.-C. Chou, and X. Xu, Topological Type-II Dirac fermions approaching the Fermi level in a transition metal dichalcogenide NiTe₂, *Chem. Mater.* 30, 4823 (2018).
- ³⁹ B. Ghosh, D. Mondal, C.-N. Kuo, C. S. Lue, J. Nayak, J. Fujii, I. Vobornik, A. Politano, and A. Agarwal, Observation of bulk states and spin-polarized topological surface states in transition metal dichalcogenide Dirac semimetal candidate NiTe₂, *Phys. Rev. B* 100, 195134 (2019).
- ⁴⁰ S. Mukherjee, S. W. Jung, S. F. Weber, C. Xu, D. Qian, X. Xu, P. K. Biswas, T. K. Kim, L. C. Chapon, M. D. Watson, J. B. Neaton, and C. Cacho, Fermi-crossing Type-II Dirac fermions and topological surface states in NiTe₂, *Sci. Rep.* 10, 12957 (2020).
- ⁴¹ J. A. Hlevyack, L.-Y. Feng, M.-K. Lin, R. A. B. Villaes, R.-Y. Liu, P. Chen, Y. Li, S.-K. Mo, F.-C. Chuang, and T.-C. Chiang, Dimensional crossover and band topology evolution in ultrathin semimetallic NiTe₂ films, *npj 2D mater. appl* 5, 40 (2021).
- ⁴² M. Nurmamat, S. V. Ereemeev, X. Wang, T. Yoshikawa, T. Kono, M. Kakoki, T. Muro, Q. Jiang, Z. Sun, M. Ye, and A. Kimura, Bulk Dirac cone and highly anisotropic electronic structure of NiTe₂, *Phys. Rev. B* 104, 155133 (2021).
- ⁴³ F. Fischer, A. Torche, M. Prada, and G. Bester, GW effects on the topology of Type-II Dirac cones in NiTe₂, PtSe₂, and PtTe₂, *Phys. Rev. B* 110, 165146 (2024).
- ⁴⁴ N. Bhatt, A. Ali, D. Sharma, S. Bansal, M. Mandal, R. P. Singh and R. S. Singh, Strongly correlated topological surface states in the type-II Dirac semimetal NiTe₂, *Phys. Rev. B* 111, 245157 (2025).
- ⁴⁵ S. Jobic, R. Brec and J. Rouxel, Anionic polymeric bonds in transition metal ditellurides, *J. Solid State Chem.* 96, 169 (1992).
- ⁴⁶ W. Bensch, W. Heid, M. Muhler, S. Jobic, R. Brec, and J. Rouxel, Anionic polymeric bonds in nickel ditelluride: crystal structure, and experimental and theoretical band structure, *J. Solid State Chem.* 121, 87 (1996).
- ⁴⁷ W. Zheng, R. Schanemann, S. Mozaffari, Y. C. Chiu, Z. B. Goraun, N. Aryal, E. Manousakis, T. M. Siegrist, K. Wei, and L. Balicas, Bulk Fermi surfaces of the Dirac type-II semimetallic candidate NiTe₂, *Phys. Rev. B* 102, 125103 (2020).
- ⁴⁸ J. Zaanen, G. Sawatzky, and J. Allen, Band gaps and electronic structure of transition-metal compounds, *Phys. Rev. Lett.* 55, 418 (1985).
- ⁴⁹ A. Prodan, F.W. Boswell., and J. M. Corbett, An electron microscopic investigation of CoTe₂ Single Crystals, *Phys. Stat. Sol.(a)* 36, K21 (1976).
- ⁵⁰ <https://www.topologicalquantumchemistry.com/>
- ⁵¹ M. W. Haverkort, M. Zwierzycki, and O. K. Andersen, Multiplet ligand-field theory using Wannier orbitals, *Phys. Rev. B* 85, 165113 (2012).
- ⁵² Y. Lu, M. Hoppner, O. Gunnarsson, and M. W. Haverkort, Efficient real-frequency solver for dynamical mean-field theory, *Phys. Rev. B* 90, 085102 (2014).
- ⁵³ M. W. Haverkort, G. Sangiovanni, P. Hansmann, A. Toschi, Y. Lu, and S. Macke, Bands, resonances, edge singularities and excitons in core level spectroscopy investigated within the dynamical mean-field theory, *EPL* 108, 57004 (2014).
- ⁵⁴ J. F. Moulder, W. F. Stickle, P. E. Sobol, and K. D. Bomben, *Handbook of X-ray Photoelectron Spectroscopy* (Perkin-Elmer Corporation, 1992).
- ⁵⁵ A complementary study on experimental and cluster model analyses of negative charge transfer correlated Dirac semi-metal CoTe₂ is submitted to *Phys. Rev. B*; arXiv:2511.03299.
- ⁵⁶ S. Nappini, D. W. Boukhvalov, G. D'Olimpio, L. Zhang, B. Ghosh, C.-N. Kuo, H. Zhu, J. Cheng, M. Nardone, L. Ottaviano, et al., Transition-metal dichalcogenide NiTe₂: An ambient-stable material for catalysis and nanoelectronics, *Adv. Funct. Mater.* 30, 2000915 (2020).
- ⁵⁷ M. Trzhaskovskaya and V. Yarzhevsky, Dirac-Fock photoionization parameters for HAXPES applications, *At. Data Nucl. Data Tables* 119, 99 (2018)
- ⁵⁸ M. Cini, Density of states of two interacting holes in a solid, *Solid State Commun.* 20, 605 (1976).
- ⁵⁹ M. Cini, Two hole resonances in the XVV Auger spectra of solids, *Solid State Commun.* 24, 681 (1977).
- ⁶⁰ G. Sawatzky, Quasiatomic Auger spectra in narrow-band metals, *Phys. Rev. Lett.* 39, 504 (1977).
- ⁶¹ P. Orders, J. Liesegang, R. Leckey, J. G. Jenkin, and J. Riley, Angle-resolved photoemission from the valence bands of NiTe₂, PdTe₂, and PtTe₂, *J. Phys. F: Met. Phys.* 12, 2737 (1982).
- ⁶² C. Guillot, Y. Ballu, J. Paigné, J. Lecante, K. Jain, P. Thiry, R. Pinchaux, Y. Petroff, and L. Falicov, Resonant photoemission in nickel metal, *Phys. Rev. Lett.* 39, 1632 (1977).
- ⁶³ M. Weinelt, A. Nilsson, M. Magnuson, T. Wiell, N. Wassdahl, O. Karis, A. Föhlisch, N. Mårtensson, J. Stöhr., and M. Samant, Resonant photoemission at the 2*p* edges of Ni: Resonant Raman and interference effects, *Phys. Rev. Lett.* 78, 967 (1997).
- ⁶⁴ S. Hüfner S.-H. Yang, B. Mun, C. Fadley, J. Schäfer, E. Rotenberg, and S. Kevan, Observation of the two-hole satellite in cr and fe metal by resonant photoemission at the 2*p* absorption energy, *Phys. Rev. B* 61, 12582 (2000).
- ⁶⁵ P. Settembri, F. Mazzola, I. Vobornik, J. Fujii, M. Kögler, C.-N. Kuo, C. S. Lue, A. Politano, and G. Profeta, Unveiling strain-responsive topological landscapes in the NiTe₂ Dirac semimetal, *Phys. Rev. B* 110, L201401 (2024).
- ⁶⁶ M. A. Veenendaal, D. Alders and G. A. Sawatzky, Influence of superexchange on Ni 2*p* x-ray absorption spectroscopy in NiO, *Phys. Rev. B* 51, 13966 (1995).
- ⁶⁷ D. Alders, L. Tjeng, F. Voogt, T. Hibma, G. Sawatzky, C. Chen, J. Vogel, M. Sacchi, and S. Iacobucci, Temperature and thickness dependence of magnetic moments in NiO epitaxial films, *Phys. Rev. B* 57, 11623 (1998).
- ⁶⁸ A. Fujimori and F. Minami, Valence-band photoemission and optical absorption in nickel compounds, *Phys. Rev. B* 30, 957(1984).
- ⁶⁹ M. A. van Veenendaal and G. A. Sawatzky, Nonlocal screening effects in 2*p* x-ray photoemission spectroscopy core-level line shapes of transition metal compounds, *Phys. Rev. Lett.* 70, 2459 (1993).
- ⁷⁰ M. Ghiasi, A. Hariki, M. Winder, J. Kunes, A. Regoutz, T.-L. Lee, Y. Hu, J.-P. Rueff, and F. M. F. de Groot, Charge-transfer effect in

- hard x-ray 1s and 2p photoemission spectra: LDA +DMFT and cluster-model analysis, *Phys. Rev. B* 100, 075146(2019).
- ⁷¹ J. Zaanen and G. A. Sawatzky, Systematics in Band Gaps and Optical Spectra of 3D Transition Metal Compounds, *Jl. Solid State Chem.* 88, 8 (1990).
- ⁷² A. E. Bocquet, T. Saitoh, T. Mizokawa and A. Fujimori, Systematics in the electronic structure of 3d transition metal compounds, *Solid State Communications* 83, 11 (1992).
- ⁷³ A. Fujimori, A. E. Bocquet, T. Saitoh and T. Mizokawa, Electronic structure of 3d transition metal compounds: systematic chemical trends and multiplet effects, *Solid State Communications* 83, 11 (1992).
- ⁷⁴ A. Fujimori, Ligand Field and Charge Transfer in Transition metal compounds, *Jl. Phys. Soc. Jpn.* 93, 121002 (2024).